Multispecies Ion Acceleration in 3D Magnetic Reconnection with Hybrid-Kinetic Simulations

Qile Zhang[*], Fan Guo, William Daughton, Hui Li, and Ari Le
Los Alamos National Laboratory, Los Alamos, New Mexico 87545, USA

Tai Phan
Space Sciences Laboratory, University of California, Berkeley, Berkeley, California 94720, USA

Mihir Desai
Southwest Research Institute, 6220 Culebra Road, San Antonio, Texas 78238, USA
and Department of Physics and Astronomy, University of Texas at San Antonio, San Antonio, Texas 78249, USA

Magnetic reconnection drives multispecies particle acceleration broadly in space and astrophysics. We perform the first 3D hybrid simulations (fluid electrons, kinetic ions) that contain sufficient scale separation to produce nonthermal heavy-ion acceleration, with fragmented flux ropes critical for accelerating all species. We demonstrate the acceleration of all ion species (up to Fe) into power-law spectra with similar indices, by a common Fermi acceleration mechanism. The upstream ion velocities influence the first Fermi reflection for injection. The subsequent onsets of Fermi acceleration are delayed for ions with lower charge-mass ratios (Q/M), until growing flux ropes magnetize them. This leads to a species-dependent maximum energy/nucleon $\propto (Q/M)^\alpha$. These findings are consistent with *in situ* observations in reconnection regions, suggesting Fermi acceleration as the dominant multispecies ion acceleration mechanism.

Introduction.—Magnetic reconnection rapidly converts magnetic energy into bulk flows, heating, and nonthermal particle acceleration. One major unsolved problem is the acceleration of energetic particles during reconnection, with broad implications to various space and astrophysical energetic phenomena [1,2]. Observations have found efficient particle acceleration during reconnection—with numerous examples from solar flares [3,4], switchbacks likely from interchange reconnection [5–7], the heliospheric current sheet (HCS) [8,9], and the magnetotail [10–13]. Often, multiple species are observed, including electrons, protons, and heavier ions [8,12,13]. These multispecies observations contain key information to discover the underlying acceleration process and can offer more stringent constraints on potential mechanisms. One important candidate is the Fermi-acceleration mechanism [14–20], where particles get accelerated through curvature drifts along motional electric fields of contracting field lines while bouncing between Alfvénic outflows. Other mechanisms have also been proposed, including the Fermi acceleration by bouncing between reconnection inflows [21–23], and parallel electric field acceleration [16,24–28].

The recent *in situ* observations measure energetic ions near reconnection layers, but the exact energization mechanisms are unknown. Parker solar probe (PSP) observations near the reconnecting HCS find multispecies energetic ions with maximum energy per nucleon $\varepsilon_{\max} \propto (Q/M)^\alpha$ where $\alpha \sim 0.65$–0.76 (M is the mass and Q is the charge) [8]. Some magnetospheric-multiscale (MMS) observations at Earth's magnetotail suggest that the ion energization is ordered by energy per charge, which indicates $\alpha \sim 1$ [12,13]. As far as we know, there have not been reconnection theories on multispecies ion acceleration that can explain these new observations. Drake *et al.* [29–31] suggested an inverse scaling ($\alpha < 0$) in the large-guide-field regime. For low guide fields, a study of plasma heating [32] suggested that the temperature is proportional to M. Mechanisms other than reconnection also face significant challenges in explaining HCS observations [8].

Fully kinetic simulations have been the primary tools for modeling particle acceleration in collisionless reconnection, as they self-consistently include key reconnection physics and feedback of energetic particles in the reconnection region. However, kinetic simulations of reconnection acceleration are still quite challenging due to the multiscale nature of the process. While several large-scale 3D fully kinetic simulations [20] have achieved efficient acceleration of electrons and protons, modeling nonthermal acceleration of heavier ions is considerably more difficult due to their large gyroradii [$\propto (Q/M)^{-1}$ at the same velocity]. Thus, nearly all previous numerical studies on

nonthermal acceleration are limited to electrons and/or protons [19,20,33,34].

Here, we employ a hybrid (self-consistent particle ions and fluid electrons) model to achieve unprecedentedly large-scale 3D kinetic simulations, to study the acceleration of multispecies ions during reconnection. Since the hybrid simulations do not need to resolve the electron inertial scale, computationally they are a factor $\sim (d_H/d_e) = (m_H/m_e)^{1/2}$ more cost efficient in each dimension per timestep than fully kinetic simulations. Here d_H, d_e, m_H, and m_e are the inertial lengths and masses of protons and electrons, respectively. Therefore hybrid simulations enable much larger domains to capture the essential physics of heavy ion acceleration. Despite the fluid approximation for electrons, hybrid simulations have demonstrated good agreement for the reconnection rate and dynamics compared to fully kinetic simulations [35–38]. In the Appendix, we show that hybrid and fully kinetic [20] simulations produce very similar proton acceleration and flux rope dynamics, demonstrating that the hybrid model is viable for studying ion acceleration.

Our hybrid simulations, for the first time, achieved efficient acceleration of multiple ion species (with a wide range of charge and mass up to $^{56}\text{Fe}^{14+}$) into nonthermal power-law energy spectra. We find that the 3D reconnection layers consist of fragmented kinking flux ropes across different scales (mainly from the $m = 1$ flux-rope kink instability), which are growing in both width and length over time, as a distinct component of the reconnection-driven turbulence. The origin and properties of reconnection-driven turbulence are frontiers of research [39–42]. Similar strong and turbulent magnetic fluctuations have also been observed in magnetotail reconnection [10,11]. This 3D dynamics plays a critical role in the particle acceleration for all species, by facilitating transport to acceleration regions. Different ions are pre-accelerated or injected into nonthermal energies when first bouncing off an Alfvénic outflow at a reconnection exhaust (a single Fermi reflection). The injection process leads to "shoulders" in the energy spectra, becoming the low-energy bounds that control the nonthermal energy content. At higher energy, all species undergo a universal Fermi acceleration process between outflows and form power-law energy spectra with similar indices ($p \sim 4.5$). However, the onset times of Fermi acceleration are delayed for lower charge-mass-ratio ions, until the flux ropes and neighboring exhausts grow large enough to magnetize them. Consequently, the maximum energy per nucleon $\varepsilon_{\max} \propto (Q/M)^\alpha$ where $\alpha \sim 0.6$ for low upstream plasma β, and both p and α increase as β approaches unity. These results are consistent with the HCS and magnetotail observations [8,12,13], suggesting that the observed energetic particles may be a natural consequence of reconnection.

Numerical simulations.—We use the Hybrid-VPIC code [43,44] that evolves multispecies ions as nonrelativistic particles and electrons as adiabatic fluid, which is coupled with Ohm's law (with small hyper-resistivity and resistivity to break the electron frozen-in condition), Ampere's law and Faraday's law. The simulations start from two identical current sheets (our analyses focus on one) with periodic boundaries and force-free profiles: $B_x = B_0\{\tanh[(z - 0.25L_z)/\lambda] - \tanh[(z - 0.75L_z)/\lambda] - 1\}$, $B_y = \sqrt{B_0^2 + B_g^2 - B_x^2}$, with uniform density and temperature. We use the initial electron density n_0 for the density normalization. B_0 is the reconnecting field, B_g is the guide field, L_z is the domain size in z, and λ is the half thickness of the sheet set to be 1 d_H. $b_g = B_g/B_0 = 0.1$ (corresponding to a magnetic shear angle 169°), which represents in general the low-guide-field regime in the HCS and magnetotail [9,45–48]. The domain size $L_x \times L_y \times L_z = 1350 \times 140.4 \times 672 d_H^3$, with grid size $\Delta x = \Delta y = \Delta z = 0.6d_H$ and 800 protons per cell (4.7×10^{11} protons in total). L_y is sufficient for capturing the $m = 1$ flux-rope kink mode for efficient acceleration [20]. Small long-wavelength perturbations are included to initiate reconnection at both current sheets. To limit the influence of periodic boundaries, the simulations terminate at time $\sim 1.3L_x/V_A$, during which less than $1/3$ of the upstream magnetic flux is reconnected and the two current sheets are not yet interacting. We include several ion species $^1\text{H}^+$, $^4\text{He}^{2+}$, $^3\text{He}^{2+}$, $^{16}\text{O}^{7+}$, $^{56}\text{Fe}^{14+}$, with abundance 95%, 5%, 0.1%, 0.1%, 0.1%, respectively. Our simulations are relevant for multi-X-line collisionless reconnection, as well as plasmoid reconnection in a thicker current sheet that may develop kinetic-scale current sheets to trigger collisionless reconnection [49–53].

We present three runs with different initial temperatures $T_i = T_e = 0.04, 0.09, 0.25 m_H V_A^2$, where $V_A = B_0/\sqrt{4\pi n_0 m_H}$ is the Alfvén speed, resulting in proton $\beta_H = 0.08, 0.18, 0.5$, respectively. We discuss the $\beta_H = 0.18$ run by default and use others for comparison. Unless otherwise stated, the simulations employ the same initial temperature for all ion species. We have performed additional simulations to confirm that the conclusions are not sensitive to different initial temperatures for different species.

Reconnection current sheet with 3D fragmented kinking flux ropes.—Figures 1(a)–1(d) shows B_z in the x–y plane in the center of one current sheet. The unprecedented 3D domain size facilitates strong $m = 1$ kink instability of flux ropes that completely fragmentizes the flux ropes—in contrast to previous smaller-domain simulations [20] with more coherent flux ropes (see Appendix). This leads to turbulent magnetic fluctuations, as in magnetotail reconnection [10,11]. As reconnection proceeds, these fragmented kinking flux ropes keep growing over time both in width and length, while they advect along the global bidirectional outflows in x. We visualize these flux ropes in 3D in Figs. 1(e)–1(f) from different perspectives. Flux ropes in (e) can be directly compared to those in (c), with the same perspective and time. Panel (f) emphasizes that
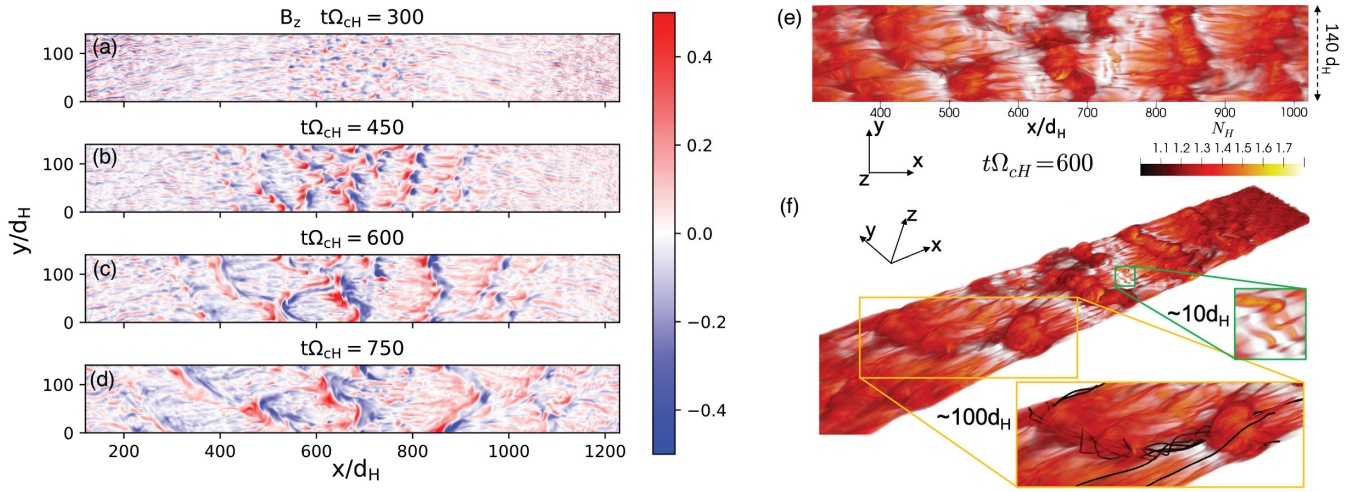
FIG. 1. (a)–(d) Magnetic field B_z in the x–y plane in the center of one current sheet ($z = 168 d_H$) at different times to show the evolution of growing fragmented kinking flux ropes. (e)–(f) Volume rendering of flux ropes in 3D using proton density at $t\Omega_{cH} = 600$ from different perspectives. Two magnified windows ($\sim 10 d_H$ and $\sim 100 d_H$) show example kinking flux ropes of vastly different scales in (f). In the $\sim 100 d_H$ window, several example field lines are shown around the flux rope to better visualize the dynamics.

flux ropes exist over a range of scales: one flux rope is newly born from the reconnection layer (green box), and another has grown to occupy a sizable fraction of the domain (orange box). This flux-rope kink instability produces chaotic field lines [20] (see also Supplemental Material [54] Fig. S1) that can diverge quickly and connect outside of the flux ropes [55,56], which enables particles to transport out of flux ropes and get further accelerated at the adjacent reconnection exhausts.

Acceleration of different ions species.—Figure 2(a) shows the particle-number spectra as a function of energy per nucleon ε for different species at the final time $t\Omega_{cH} = 1800$ (solid lines) normalized by their abundance ratio to Fe. For the first time, the simulation shows that all ion species are accelerated into power-law spectra with similar indices $p \sim 4.5$, suggesting a universal acceleration process across different ion species. Over time, these nonthermal

power laws are formed with sustainable slopes and keep extending to higher energy (Supplemental Material [54] Fig. S2). Moreover, each species develops a shoulder feature in the spectra, marking the low energy bounds of power laws at somewhat different energies. This feature indicates a similar injection process for each species but with intriguing differences, as we will discuss below. We obtain ε_{max} as the power-law high-energy cutoffs (where the spectra deviate from the fitted power laws by an e-fold) and show the relative values near the final time in Fig. 2(b), which follows a fitted scaling $\varepsilon_{max} \propto (Q/M)^\alpha$ ($\alpha \sim 0.65$). A simulation with lower $\beta_H = 0.08$ produces similar $p \sim 4.0$ and $\alpha \sim 0.54$, suggesting a low-β limit, while another simulation with higher $\beta_H = 0.5$ approaching unity produces $p \sim 6.3$ and $\alpha \sim 1.14$. We also performed corresponding 2D simulations and find less efficient acceleration than 3D (Supplemental Material [54] Fig. S3),
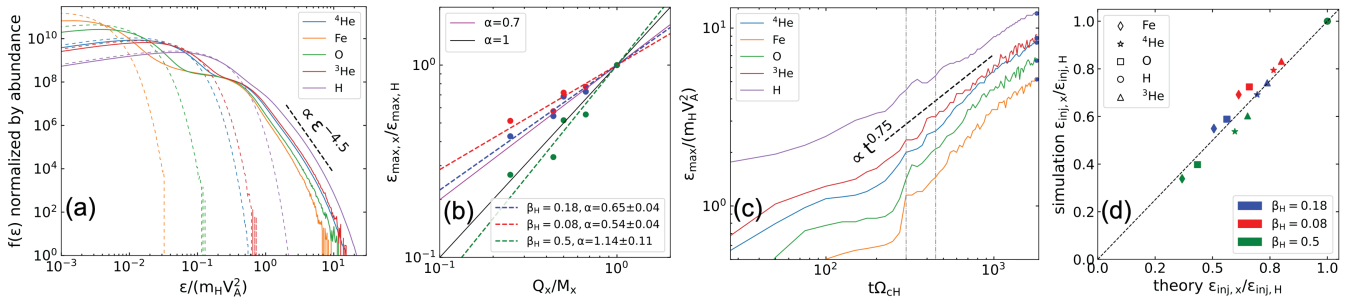

FIG. 2. (a) Final particle-number spectra (solid lines) normalized by the abundance ratio to Fe, versus energy per nucleon ε. The initial spectra (dash lines) are also shown for reference. (b) Maximum energy per nucleon ε_{max} for each species normalized by that of Hydrogen (averaged over time near $t\Omega_{cH} = 1800$) versus charge-to-mass ratio, shown for three β_H cases. The red, blue, and green dashed lines fit $(Q_x/M_x)^\alpha$ for different cases, and the fitted α and standard errors are listed in legend. Two solid reference lines $\alpha = 0.7, 1.0$ indicate different observations [8,12,13]. (c) ε_{max} versus time for $\beta_H = 0.18$. Blue dots are marked at $t\Omega_{cH} = 1800$ to indicate the values used in (b). Two vertical gray lines indicate two times evaluated in Fig. 3. (d) Theoretical estimates of the injection energies (shoulders) normalized by that of hydrogen, versus those obtained in simulations at $t\Omega_{cH} = 1800$.

showing that the 3D dynamics above are critical for particle acceleration of all species.

The time evolution of $\varepsilon_{\max}$ [Fig. 2(c)] features a common evolution pattern across different species. Different $\varepsilon_{\max}$ first increase to $\sim m_H V_A^2$ close to the shoulders in Fig. 2(a), entering the nonthermal energies (injection). Later on, different $\varepsilon_{\max}$ start increasing at a similar slope roughly following $\varepsilon_{\max} \propto t^{0.75}$, once again indicating a universal acceleration process. Simulations with different domain sizes show that the final $\varepsilon_{\max}$ is only limited by the acceleration time ($\propto L_x/V_A$). Intriguingly, lower Q/M ions have delayed transitions into the acceleration phase, leading to lower final $\varepsilon_{\max}$. Because of the similar acceleration slope, the relative ratios of $\varepsilon_{\max}$ between two species will preserve over time and domain sizes, so the ratios in our simulations can extend to larger scales. Our simulation results are consistent with PSP observations near the HCS [8] where upstream $\beta_H \sim 0.2$, $\alpha \sim 0.65$–0.76 [see Fig. 2(b) $\alpha = 0.7$ as a reference line] and $p \sim 4$–6 (similar between species considering observational uncertainty). In MMS observations near the magnetotail [12,13] where upstream β_H (usually < 1) is difficult to measure precisely, the inferred $\alpha \sim 1$ and $p \sim 5$–6 are comparable to our simulation results [Fig. 2(b) $\alpha = 1$].

Particle injection and acceleration mechanisms.—We find that all species are accelerated by a common Fermi acceleration process, with their acceleration rates arising from curvature drifts [15,17] (not shown). We demonstrate the repeated Fermi bounces between outflows with tracer particles in Supplemental Material [54] [Fig. S4(a)]. This process produces similar spectral indices $p \sim 4.5$ and acceleration $\varepsilon \propto t^{0.75}$ for protons and heavier ions up to ^{56}Fe^{14+}. To our knowledge, this is the first kinetic study demonstrating clear Fermi acceleration of heavier ions. While heavier ions have large gyroradii, the Fermi process can still operate at scales larger than their gyro-motion. We also find that a higher initial β approaching unity can steepen the power laws by weakening field-line contraction associated with Fermi acceleration. On the one hand, we observed that an initial pressure approaching the magnetic pressure reduces the compression or shrinking at flux ropes related to field-line contraction [18]. On the other hand, this high initial pressure facilitates Fermi acceleration (proportional to parallel energy) that boost the parallel pressure. Therefore, it weakens the firehose parameter $F_h = 1 - 4\pi(P_\parallel - P_\perp)/B^2$ (observed in our simulations) and thus field-line tension ($F_h \mathbf{B} \cdot \nabla \mathbf{B}/4\pi$) that drives field-line contraction [34]. We have performed additional simulations with different initial temperatures (0.09–$0.25 m_H V_A^2$) for the minor ions, and find little changes (< 0.2) in the spectral slopes. This is because minor ions contribute very little pressure, and can hardly affect the contracting field lines for Fermi acceleration that determines their power-law slopes.

Before Fermi acceleration, all ion species can be injected through a Fermi reflection when first crossing an exhaust [Supplemental Material [54] Fig. S4(a-b)], but are influenced by their initial thermal velocities $V_{th} = \sqrt{T_0/M}$ (lower for heavier ions). A particle around the initial thermal velocity will get kicked by the exhaust and gain twice of the outflow speed. Taking the typical outflow speed measured in the simulation (with $\beta_H = 0.18$) $V_{out} \sim 0.6V_A$, we can roughly estimate the injection energy per nucleon from a single Fermi reflection

$$\varepsilon_{inj} \sim 0.5 m_H (2V_{th} + 2V_{out})^2 = 2m_H(V_{th} + V_{out})^2. \quad (1)$$

We have used initial velocity $2V_{th}$ near the higher-energy drop-off of the initial Maxwellian energy spectra, which will approximately correspond to the shoulder after the Fermi reflection. This theoretical estimate agrees approximately with the shoulders in Fig. 2(a) (determined at a level 10^7), as demonstrated in Fig. 2(d).

The delayed onset of Fermi acceleration for lower Q/M ions is caused by their larger gyroradii after injection: they get magnetized at later times when flux ropes and their adjacent exhausts grow large enough. We demonstrate this in Fig. 3 with the density of several ion species (normalized by their initial density) beyond their injection energies [Eq. (1)] at different times [gray lines in Fig. 2(c)], around the region filled with flux ropes. At $t\Omega_{cH} = 300$, with relatively small flux ropes ($\sim 5d_H$ in z), protons (post-injection gyroradius $\rho_H \sim 1.4d_H$ taking $\varepsilon_{inj} \sim 1m_H V_A^2$) have already started Fermi acceleration for some time with many particles beyond the injection energy, while ^{3}He just started, and most Oxygens (postinjection $\rho_O \sim 3.2d_H$) are not accelerated. At $t\Omega_{cH} = 450$ the flux ropes become larger ($\sim 10d_H$ in z) and all ion species are magnetized after injection, allowing continuous Fermi acceleration. Note that there is a short-term $\varepsilon_{\max}$ increase before $t\Omega_{ci} = 300$ [Fig. 2(c)] for all species distinct from Fermi acceleration, more apparent for heavy ions. This is because a far-downstream portion (hundreds of d_H from the x line) of the large exhausts at this early time reaches a somewhat higher exhaust speed ($\sim 0.8V_A$). At later time after the exhausts break up into flux ropes, this effect vanishes and gets overwhelmed by Fermi acceleration.

To further elucidate this mechanism, we perform the following scaling analysis. The gyroradius after injection $\rho_x \propto (Q_x/M_x)^{-1}\sqrt{\varepsilon_{inj,x}}$ for a species x, with $\varepsilon_{inj,x}$ given in Eq. (1). Assuming flux ropes grow linearly over time, the starting time of magnetization and acceleration $t_0 \propto (Q_x/M_x)^{-1}\sqrt{\varepsilon_{inj,x}}$. During Fermi acceleration we set

$$\varepsilon_{\max,x} \sim C_x t^\gamma, \quad (2)$$

where C_x is a species-specific constant. Since $\varepsilon_{\max} = \varepsilon_{inj}$ at $t = t_0$, we obtain
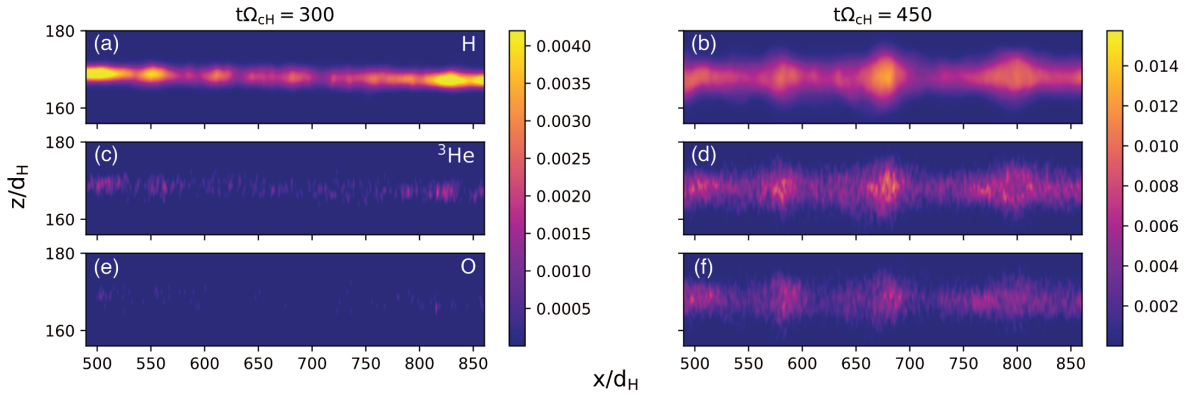
FIG. 3. The energetic particles density above injection energy (H—top, ^{3}He—middle, O—bottom) in the $x - z$ plane (averaged over y) at 2 times.

$$\varepsilon_{\max,x}/\varepsilon_{\max,H} \propto C_x/C_H \propto (Q_x/M_x)^\gamma \left(\frac{\varepsilon_{\text{inj},x}}{\varepsilon_{\text{inj},H}}\right)^{1-\gamma/2}. \quad (3)$$

When $\beta \ll 1$, $(\varepsilon_{\text{inj},x}/\varepsilon_{\text{inj},H})^{1-\gamma/2} \sim 1$. Since the fitted scaling $\varepsilon_{\max,x}/\varepsilon_{\max,H} \propto (Q_x/M_x)^\alpha$, we have α related to the acceleration exponent: $\alpha \sim \gamma$. In our low-β simulations, $\gamma \sim 0.75$ [Fig. 2(c)] roughly agrees with $\alpha \sim 0.6$ [Fig. 2(b)]. A higher initial β approaching unity will introduce corrections since $(\varepsilon_{\text{inj},x}/\varepsilon_{\text{inj},H})^{1-\gamma/2} < 1$ in Eq. (3), increasing the relative difference of $\varepsilon_{\max}$ and therefore α. Since γ may also change with β, a more detailed understanding will require future study. Note that Eq. (2) implies the maximum gyroradius scales in time as $\rho_{\max,x} \propto \sqrt{\varepsilon_{\max,x}} \propto t^{\gamma/2} \sim t^{0.38}$, which grows much slower than flux ropes ($\propto t$), enabling the highest energy particles to stay magnetized during Fermi acceleration.

Discussion and conclusion.—In summary, our 3D hybrid simulations demonstrate simultaneous nonthermal acceleration of all available ion species (up to ^{56}Fe^{14+}) in magnetic reconnection. We have uncovered the 3D turbulent dynamics and the fundamental mechanisms of particle injection and acceleration for multispecies ion acceleration, with strong implications to not only heliophysics but also astrophysics—such as stellar flares and accretion-disk flares [57,58] with nonrelativistic or transrelativistic magnetization. In a real system with open boundaries and escape of magnetic flux, reconnection can keep occurring to produce new flux ropes, so the dynamics in our simulations can occur repeatedly, rather than being transient.

Our hybrid simulations only take into account the electron adiabatic heating without electron acceleration and pressure anisotropy, which can potentially influence magnetic tension and energy release. We also neglect potential electron-driven instabilities that affect ion acceleration, e.g., [59], which needs further studies. However, previous studies suggest that electrons have less energy gain and pressure anisotropy than protons in reconnection [20,24,25,27,60–62] due to weaker gain from

Fermi reflection. In the Appendix, hybrid simulations indeed produce proton spectra similar to fully kinetic simulations [20].

Our predicted spectrum features (p, α) may naturally account for the current observations near HCS and the magnetotail with low guide fields. While the HCS observation [8] (from PSP encounter 7) has a peak ion intensity occurring just outside the reconnection exhaust, this is not a common feature for HCS crossings. More recent PSP encounters such as 10 and 11 have found peak intensities inside the exhausts [63]. The observed profiles are likely affected by not only acceleration but also transport, and therefore may be highly variable across encounters. Detailed comparisons with simulations will require a future statistical study with many crossings beyond the scope of this Letter. The remote sources like interchange reconnection and solar flares need to be further explored, where parameters are much less constrained, e.g., [64]. The 3D flux-rope dynamics and the dependence of features (such as $p, \alpha, \varepsilon_{inj}$) on parameters can be compared in details with future spacecraft measurements, which is critical for understanding particle acceleration in reconnection.
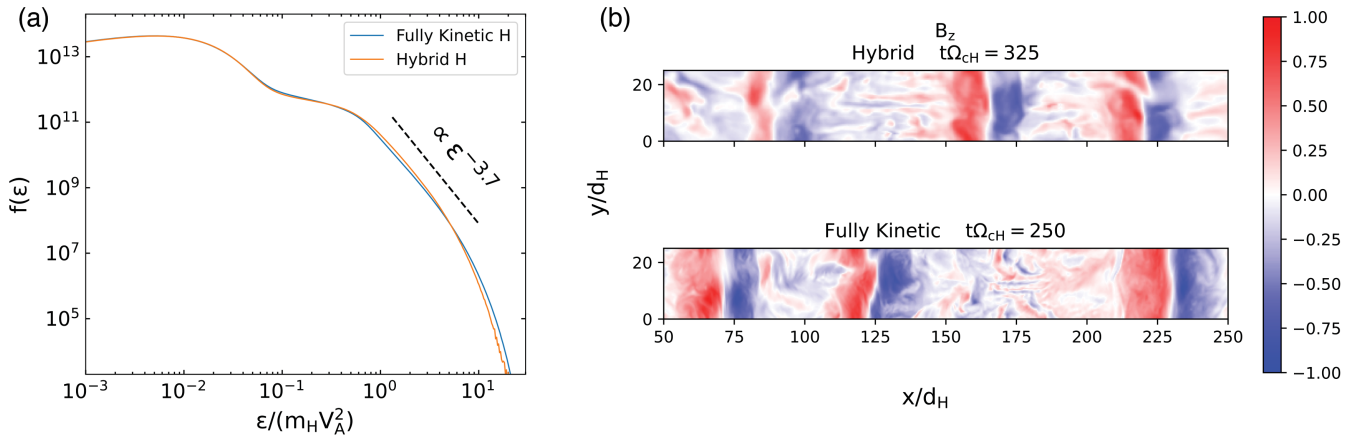
FIG. 4.   Comparison of hybrid and fully kinetic simulations with parameters $L_x = 300d_H$, $L_y = 25d_H$, $b_g = 0.2$, $T = 0.01m_HV_A^2$. (a) Proton spectra (normalized to have the same total number) when hybrid ($t\Omega_{cH} = 475$) and fully kinetic ($t\Omega_{cH} = 400$) runs have similar reconnected magnetic flux. (b) Comparison of magnetic flux ropes by showing B_z on a x-y cut in the middle of the reconnection layer at simulation times when hybrid ($t\Omega_{cH} = 325$) and fully kinetic ($t\Omega_{cH} = 250$) runs have similar reconnected magnetic flux.

Appendix: Comparing hybrid and fully kinetic simulations.—We show here a direct comparison of the hybrid and the fully kinetic [20] simulations, and their results are very similar. We use the same physical parameters in [20] for the hybrid simulation: $L_x = 300d_H$, $L_y = 25d_H$, $b_g = 0.2$, $T = 0.01m_HV_A^2$, with only the proton ion species. Because of the double periodic setup for the hybrid code, we use $L_z = 250d_H$ for the hybrid run, which doubles $L_z = 125d_H$ of the fully kinetic run. We compare snapshots from both runs at times with similar reconnected magnetic flux. As shown in Fig. 4, the proton energy spectra for both runs closely resemble each other. As for the flux rope dynamics, both runs have kink unstable flux ropes but they are more coherent (not fragmented) due to the small domain size compared to those with large domains in Fig. 1.

*qlzhang@lanl.gov

[1] M. Yamada, R. Kulsrud, and H. Ji, Magnetic reconnection, Rev. Mod. Phys. **82**, 603 (2010).

[2] J. Ambrosiano, W. H. Matthaeus, M. L. Goldstein, and D. Plante, Test particle acceleration in turbulent reconnecting magnetic fields, Geophys. Res. Lett. **93**, 14383 (1988).

[3] G. M. Mason *et al.*, 3he-rich solar energetic particle events observed on the first perihelion pass of solar orbiter, Astron. Astrophys. **656**, L1 (2021).

[4] C. M. S. Cohen *et al.*, Parker solar probe observations of He/H abundance variations in SEP events inside 0.5 AU, Astron. Astrophys. **650**, A23 (2021).

[5] S. D. Bale *et al.*, A solar source of Alfvénic magnetic field switchbacks: In situ remnants of magnetic funnels on supergranulation scales, Astrophys. J. **923**, 174 (2021).

[6] S. D. Bale, J. F. Drake, M. D. McManus, M. I. Desai, S. T. Badman, D. E. Larson, M. Swisdak, T. S. Horbury, N. E. Raouafi, T. Phan, M. Velli, D. J. McComas, C. M. S. Cohen, D. Mitchell, O. Panasenco, and J. C. Kasper, Interchange reconnection as the source of the fast solar wind within coronal holes, Nature (London) **618**, 252 (2023).

[7] J. F. Drake, O. Agapitov, M. Swisdak, S. T. Badman, S. D. Bale, T. S. Horbury, J. C. Kasper, R. J. MacDowall, F. S. Mozer, T. D. Phan, M. Pulupa, A. Szabo, and M. Velli, Switchbacks as signatures of magnetic flux ropes generated by interchange reconnection in the corona, Astron. Astrophys. **650**, A2 (2021).

[8] M. I. Desai *et al.*, Suprathermal ion energy spectra and anisotropies near the heliospheric current sheet crossing observed by the Parker solar probe during encounter 7, Astrophys. J. **927**, 62 (2022).

[9] T. D. Phan *et al.*, Parker solar probe observations of solar wind energetic proton beams produced by magnetic reconnection in the near-sun heliospheric current sheet, Geophys. Res. Lett. **49**, e96986 (2022).

[10] R. E. Ergun *et al.*, Magnetic reconnection, turbulence, and particle acceleration: Observations in the Earth's magnetotail, **45**, 3338 (2018).

[11] R. E. Ergun *et al.*, Observations of particle acceleration in magnetic reconnection-driven turbulence, Astrophys. J. **898**, 154 (2020).

[12] S. T. Bingham, I. J. Cohen, B. H. Mauk, D. L. Turner, D. G. Mitchell, S. K. Vines, S. A. Fuselier, R. B. Torbert, and J. L. Burch, Charge-state-dependent energization of suprathermal ions during substorm injections observed by MMS in the magnetotail, J. Geophys. Res. **125**, e28144 (2020).

[13] L. Richard, Y. V. Khotyaintsev, D. B. Graham, A. Vaivads, R. Nikoukar, I. J. Cohen, D. L. Turner, S. A. Fuselier, and C. T. Russell, Proton and helium ion acceleration at magnetotail plasma jets, J. Geophys. Res. **127**, e2022JA030430 (2022).

[14] J. F. Drake, M. Swisdak, H. Che, and M. A. Shay, Electron acceleration from contracting magnetic islands during reconnection, Nature (London) **443**, 553 (2006).

[15] J. T. Dahlin, J. F. Drake, and M. Swisdak, The mechanisms of electron heating and acceleration during magnetic reconnection, Phys. Plasmas **21,** 092304 (2014).

[16] J. T. Dahlin, J. F. Drake, and M. Swisdak, The role of three-dimensional transport in driving enhanced electron acceleration during magnetic reconnection, Phys. Plasmas **24,** 092110 (2017).

[17] X. Li, F. Guo, H. Li, and G. Li, Particle acceleration during magnetic reconnection in a low-beta plasma, Astrophys. J. **843,** 21 (2017).

[18] X. Li, F. Guo, H. Li, and J. Birn, The roles of fluid compression and shear in electron energization during magnetic reconnection, Astrophys. J. **855,** 80 (2018).

[19] X. Li, F. Guo, H. Li, A. Stanier, and P. Kilian, Formation of power-law electron energy spectra in three-dimensional low-β magnetic reconnection, Astrophys. J. **884,** 118 (2019).

[20] Q. Zhang, F. Guo, W. Daughton, H. Li, and X. Li, Efficient nonthermal ion and electron acceleration enabled by the flux-rope kink instability in 3d nonrelativistic magnetic reconnection, Phys. Rev. Lett. **127,** 185101 (2021).

[21] E. M. de Gouveia dal Pino and A. Lazarian, Production of the large scale superluminal ejections of the microquasar GRS 1915 + 105 by violent magnetic reconnection, Astron. Astrophys. **441,** 845 (2005).

[22] A. Lazarian, L. Vlahos, G. Kowal, H. Yan, A. Beresnyak, and E. M. de Gouveia Dal Pino, Turbulence, magnetic reconnection in turbulent fluids and energetic particle acceleration, Space Sci. Rev. **173,** 557 (2012).

[23] A. Lazarian, G. L. Eyink, A. Jafari, G. Kowal, H. Li, S. Xu, and E. T. Vishniac, 3D turbulent reconnection: Theory, tests, and astrophysical implications, Phys. Plasmas **27,** 012305 (2020).

[24] Q. Zhang, J. F. Drake, and M. Swisdak, Particle heating and energy partition in low-β guide field reconnection with kinetic Riemann simulations, Phys. Plasmas **26,** 072115 (2019).

[25] Q. Zhang, J. F. Drake, and M. Swisdak, Instabilities and turbulence in low-β guide field reconnection exhausts with kinetic Riemann simulations, Phys. Plasmas **26,** 102115 (2019).

[26] A. Le, J. Egedal, W. Daughton, W. Fox, and N. Katz, Equations of state for collisionless guide-field reconnection, Phys. Rev. Lett. **102,** 085001 (2009).

[27] C. C. Haggerty, M. A. Shay, J. F. Drake, T. D. Phan, and C. T. McHugh, The competition of electron and ion heating during magnetic reconnection, Geophys. Res. Lett. **42,** 9657 (2015).

[28] L. Comisso and L. Sironi, Particle acceleration in relativistic plasma turbulence, Phys. Rev. Lett. **121,** 255101 (2018).

[29] J. F. Drake, P. A. Cassak, M. A. Shay, M. Swisdak, and E. Quataert, A magnetic reconnection mechanism for ion acceleration and abundance enhancements in impulsive flares, Astrophys. J. **700,** L16 (2009).

[30] J. F. Drake and M. Swisdak, The onset of ion heating during magnetic reconnection with a strong guide field, Phys. Plasmas **21,** 072903 (2014).

[31] K. Knizhnik, M. Swisdak, and J. F. Drake, The acceleration of ions in solar flares during magnetic reconnection, Astrophys. J. **743,** L35 (2011).

[32] J. F. Drake, M. Swisdak, T. D. Phan, P. A. Cassak, M. A. Shay, S. T. Lepri, R. P. Lin, E. Quataert, and T. H. Zurbuchen, Ion heating resulting from pickup in magnetic reconnection exhausts, J. Geophys. Res. **114,** A05111 (2009).

[33] F. Guo, H. Li, W. Daughton, and Y.-H. Liu, Formation of hard power laws in the energetic particle spectra resulting from relativistic magnetic reconnection, Phys. Rev. Lett. **113,** 155005 (2014).

[34] H. Arnold, J. F. Drake, M. Swisdak, F. Guo, J. T. Dahlin, B. Chen, G. Fleishman, L. Glesener, E. Kontar, T. Phan, and C. Shen, Electron acceleration during macroscale magnetic reconnection, Phys. Rev. Lett. **126,** 135101 (2021).

[35] A. Stanier, W. Daughton, L. Chacón, H. Karimabadi, J. Ng, Y.-M. Huang, A. Hakim, and A. Bhattacharjee, Role of ion kinetic physics in the interaction of magnetic flux ropes, Phys. Rev. Lett. **115,** 175004 (2015).

[36] A. Stanier, W. Daughton, A. N. Simakov, L. Chacón, A. Le, H. Karimabadi, J. Ng, and A. Bhattacharjee, The role of guide field in magnetic reconnection driven by island coalescence, Phys. Plasmas **24,** 022124 (2017).

[37] A. Le, W. Daughton, H. Karimabadi, and J. Egedal, Hybrid simulations of magnetic reconnection with kinetic ions and fluid electron pressure anisotropy, Phys. Plasmas **23,** 032114 (2016).

[38] J. Birn, J. F. Drake, M. A. Shay, B. N. Rogers, R. E. Denton, M. Hesse, M. Kuznetsova, Z. W. Ma, A. Bhattacharjee, A. Otto, and P. L. Pritchett, Geospace Environmental Modeling (GEM) magnetic reconnection challenge, J. Geophys. Res. **106,** 3715 (2001).

[39] A. Beresnyak, Three-dimensional spontaneous magnetic reconnection, Astrophys. J. **834,** 47 (2017).

[40] G. Kowal, D. A. Falceta-Gonçalves, A. Lazarian, and E. T. Vishniac, Statistics of reconnection-driven turbulence, Astrophys. J. **838,** 91 (2017).

[41] Y.-M. Huang and A. Bhattacharjee, Turbulent magnetohydrodynamic reconnection mediated by the plasmoid instability, Astrophys. J. **818,** 20 (2016).

[42] G. Kowal, D. A. Falceta-Gonçalves, A. Lazarian, and E. T. Vishniac, Kelvin-helmholtz versus tearing instability: What drives turbulence in stochastic reconnection?, Astrophys. J. **892,** 50 (2020).

[43] A. Le, D. Winske, A. Stanier, W. Daughton, M. Cowee, B. Wetherton, and F. Guo, Astrophysical explosions revisited: Collisionless coupling of debris to magnetized plasma, J. Geophys. Res. **126,** e29125 (2021).

[44] K. J. Bowers, B. J. Albright, L. Yin, B. Bergen, and T. J. T. Kwan, Ultrahigh performance three-dimensional electromagnetic relativistic kinetic plasma simulation, Phys. Plasmas **15,** 055703 (2008).

[45] T. D. Phan *et al.*, Prevalence of magnetic reconnection in the near-Sun heliospheric current sheet, Astron. Astrophys. **650,** A13 (2021).

[46] R. B. Torbert *et al.*, Electron-scale dynamics of the diffusion region during symmetric magnetic reconnection in space, Science **362,** 1391 (2018).

[47] M. Øieroset, T. D. Phan, M. Fujimoto, R. P. Lin, and R. P. Lepping, In situ detection of collisionless reconnection in the Earth's magnetotail, Nature (London) **412,** 414 (2001).

[48] L. J. Chen, S. Wang, M. Hesse, R. E. Ergun, T. Moore, B. Giles, N. Bessho, C. Russell, J. Burch, R. B. Torbert, K. J. Genestreti, W. Paterson, C. Pollock, B. Lavraud, O. Le Contel, R. Strangeway, Y. V. Khotyaintsev, and P. A. Lindqvist, Electron diffusion regions in magnetotail reconnection under varying guide fields, Geophys. Res. Lett. **46,** 6230 (2019).

[49] K. Shibata and S. Tanuma, Plasmoid-induced-reconnection and fractal reconnection, Earth, Planets, Space **53,** 473 (2001).

[50] L. Comisso, M. Lingam, Y. M. Huang, and A. Bhattacharjee, Plasmoid instability in forming current sheets, Astrophys. J. **850,** 142 (2017).

[51] D. A. Uzdensky and N. F. Loureiro, Magnetic reconnection onset via disruption of a forming current sheet by the tearing instability, Phys. Rev. Lett. **116,** 105003 (2016).

[52] W. Daughton, V. Roytershteyn, B. J. Albright, H. Karimabadi, L. Yin, and K. J. Bowers, Transition from collisional to kinetic regimes in large-scale reconnection layers, Phys. Rev. Lett. **103,** 065004 (2009).

[53] H. Ji and W. Daughton, Phase diagram for magnetic reconnection in heliophysical, astrophysical, and laboratory plasmas, Phys. Plasmas **18,** 111207 (2011).

[54] See Supplemental Material at http://link.aps.org/supplemental/10.1103/PhysRevLett.132.115201 for 3D effects, particle injection and acceleration processes.

[55] L. Yang, H. Li, F. Guo, X. Li, S. Li, J. He, L. Zhang, and X. Feng, Fast magnetic reconnection with turbulence in high Lundquist number limit, Astrophys. J.**901,** L22 (2020).

[56] F. Guo, X. Li, W. Daughton, H. Li, P. Kilian, Y.-H. Liu, Q. Zhang, and H. Zhang, Magnetic energy release, plasma dynamics, and particle acceleration in relativistic turbulent magnetic reconnection, Astrophys. J. **919,** 111 (2021).

[57] B. Ripperda, F. Bacchini, and A. A. Philippov, Magnetic reconnection and hot spot formation in black hole accretion disks, Astrophys. J. **900,** 100 (2020).

[58] A. Nathanail, C. M. Fromm, O. Porth, H. Olivares, Z. Younsi, Y. Mizuno, and L. Rezzolla, Plasmoid formation in global GRMHD simulations and AGN flares, Mon. Not. R. Astron. Soc. **495,** 1549 (2020).

[59] L. A. Fisk, ^{3}He-rich flares: A possible explanation, Astrophys. J. **224,** 1048 (1978).

[60] T. D. Phan, M. A. Shay, J. T. Gosling, M. Fujimoto, J. F. Drake, G. Paschmann, M. Øieroset, J. P. Eastwood, and V. Angelopoulos, Electron bulk heating in magnetic reconnection at Earth's magnetopause: Dependence on the inflow Alfvén speed and magnetic shear, Geophys. Res. Lett. **40,** 4475 (2013).

[61] T. D. Phan, J. F. Drake, M. A. Shay, J. T. Gosling, G. Paschmann, J. P. Eastwood, M. Øieroset, M. Fujimoto, and V. Angelopoulos, Ion bulk heating in magnetic reconnection exhausts at earth's magnetopause: Dependence on the inflow alfvén speed and magnetic shear angle, Geophys. Res. Lett. **41,** 7002 (2014).

[62] M. A. Shay, C. C. Haggerty, T. D. Phan, J. F. Drake, P. A. Cassak, P. Wu, M. Øieroset, M. Swisdak, and K. Malakit, Electron heating during magnetic reconnection: A simulation scaling study, Phys. Plasmas **21,** 122902 (2014).

[63] M. I. Desai et al., Suprathermal ion observations associated with the heliospheric current sheet crossings by Parker solar probe during encounters 7-11, in *AGU Fall Meeting Abstracts* (American Geophysical Union, Washington, D.C., 2022), Vol. 2022, pp. SH32E–1809.

[64] J. T. Dahlin, S. K. Antiochos, J. Qiu, and C. R. DeVore, Variability of the reconnection guide field in solar flares, Astrophys. J. **932,** 94 (2022).